

BIOPHYSICS

An interaction network in the polymerase active site is a prerequisite for Watson-Crick base pairing in Pol γ

Joon Park^{1,2†}, Geoffrey K. Herrmann^{1,2‡}, Arkanil Roy³, Christie K. Shumate^{4§},
G. Andrés Cisneros^{3,5*}, Y. Whitney Yin^{1,2,4*}

The replication accuracy of DNA polymerase gamma (Pol γ) is essential for mitochondrial genome integrity. Mutation of human Pol γ arginine-853 has been linked to neurological diseases. Although not a catalytic residue, Pol γ arginine-853 mutants are void of polymerase activity. To identify the structural basis for the disease, we determined a crystal structure of the Pol γ mutant ternary complex with correct incoming nucleotide 2'-deoxycytidine 5'-triphosphate (dCTP). Opposite to the wild type that undergoes open-to-closed conformational changes when bound to a correct nucleotide that is essential for forming a catalytically competent active site, the mutant complex failed to undergo the conformational change, and the dCTP did not base pair with its Watson-Crick complementary templating residue. Our studies revealed that arginine-853 coordinates an interaction network that aligns the 3'-end of primer and dCTP with the catalytic residues. Disruption of the network precludes the formation of Watson-Crick base pairing and closing of the active site, resulting in an inactive polymerase.

INTRODUCTION

Mitochondrial genome integrity is essential for cellular energy supplies and metabolism. Accurate replication of mitochondrial DNA (mtDNA) relies on the high-fidelity DNA polymerase gamma (Pol γ) to faithfully copy the parental DNA to the daughter strands. Human Pol γ coordinates the activity of DNA synthesis in its polymerase (Pol) site with self-error correction in the exonuclease (Exo) site to maintain high replication precision (1–3). Mutations in Pol γ have been implicated in neurological and muscular disorders, and exo-deficient variants lead to premature aging [see review (4)].

The accuracy of high-fidelity DNA polymerases is attributed to their ability to select a correct nucleotide from a mixed pool of nucleotides and to proofread any misincorporation. As the correct nucleotide only differs from incorrect ones at the nucleobase, the current view of fidelity is centered on the base selection via Watson-Crick base pairing, and binding to the correct nucleotide induces the obligatory open-to-closed conformational changes to form a catalytic competent *pol* active site. The base complementarity in fidelity is necessary, but is it sufficient in inducing conformational change and reconfiguring the active site?

Pol γ mutations, R853Q and R853W, result in devastating neurological disorders (5–9). Arg⁸⁵³ is not a catalytic residue, yet its substitution for Gln is completely void of polymerase activity (10). To investigate the structural basis of the catalytically deficient mutants, we determined a crystal structure of the Pol γ R853A mutant ternary complex with a primer/template DNA and a correct incoming nucleotide, as well as a cryo-electron microscopy (cryo-EM) structure of the wild-type (WT) Pol γ binary complex without bound deoxynucleotide triphosphate

(dNTP). The structures revealed an interaction network around Arg⁸⁵³ that aligns the catalytic residues with reactants—the 3'-end of the primer and dNTP. The Arg⁸⁵³ forms a hydrogen bond with the ribose moiety of dNTP. The mutant Pol γ ternary complex, although bound to the correct dNTP, adopts an open conformation. Our molecular dynamics (MD) analysis showed that Arg⁸⁵³ substitution destabilizes the Pol site and alters the energetic landscape of the polymerase. Our results showed that an Arg⁸⁵³-coordinated interaction network in the Pol site and its interaction with the ribose moiety are prerequisites for Watson-Crick base pair formation and closing of the active site.

RESULTS

Void of polymerase activity in Pol γ R853X mutants

Pol γ 's catalytic subunit, Pol γ A, WT or its variants (R853A, R853Q, or R853W), and WT Pol γ B were purified separately to greater than 95% homogeneity and mixed to form a holoenzyme for DNA synthesis assays (Fig. 1). The Pol γ holoenzyme was incubated with equimolar amount of a 5'-6FAM-25-nucleotide (nt) primer annealed to 45-nt template (24 nt/45 nt) duplex (Fig. 1). The reactions were initiated with addition of dNTPs and Mg²⁺. Within 1 min, WT Pol γ extended nearly all primer to the full-length 45-nt product and produced only a trace amount of the shortened primer (Fig. 1, lane 2), whereas R853A, R853Q, and R853W variants failed to produce any synthesis products (Fig. 1, lanes 5, 9, and 12). At 60 min, the full-length 45-nt product was shortened by a few nucleotides in the presence of the WT enzyme, likely due to the slow Exo hydrolysis of the correctly matched 45-base pair double-stranded DNA. In contrast, regardless of the substitution, all Pol γ mutants excised the primer to mostly single and dinucleotides, indicating the lack of Arg⁸⁵³ causes a severe imbalance in Pol and Exo activities. The lack of Pol activity is not caused by elevated Exo activity as Pol γ carrying R853A/Q mutants did not exhibit DNA synthesis activity (10, 11).

Pol γ binary complex structure to complete in a single-nucleotide incorporation cycle

To pinpoint the structural defect for Pol γ Arg⁸⁵³ substitution reducing the polymerization function, we first completed the structural characterization of a nucleotide incorporation reaction catalyzed by

¹Department of Biochemistry and Molecular Biology, University of Texas Medical Branch, Galveston, TX 77555, USA. ²Sealy Center for Structural Biology and Molecular Biophysics, University of Texas Medical Branch, Galveston, TX 77555, USA. ³Department of Chemistry and Biochemistry, University of Texas at Dallas, Richardson, TX 75080, USA. ⁴Department of Pharmacology and Toxicology, University of Texas Medical Branch, Galveston, TX 77555, USA. ⁵Department of Physics, University of Texas at Dallas, Richardson, TX 75080, USA.

*Corresponding author. Email: andres@utdallas.edu (G.A.C.); ywyin@utmb.edu (Y.W.Y.)
†These authors contributed equally to this work.

‡Present address: Verna and Marrs McLean Department of Biochemistry and Molecular Biology, Baylor College of Medicine, Houston, TX 77030, USA.

§Present address: Department of Psychiatry and Behavioral Science, University of Texas Health Science Center at Houston, Houston, TX 77030, USA.

WT Pol γ , which begins with the apo enzyme binding to a primer/template DNA (DNA_n) to form a binary complex, and then iterates through the three-step cycle: binding of incoming nucleotide in the N-site to form a ternary complex, extending the DNA_n primer in the P-site to DNA_{n+1} in the N-site by nucleotidyl transfer reaction, and translocating the newly synthesized primer back to the P-site with subsequent release of pyrophosphate (Fig. 2).

As structures of Pol γ apo enzyme and ternary complex were previously determined (11–13), we here determined the structure of Pol γ -DNA binary complex using cryo-EM. A homogeneous, a single population was resolved, and the structure was refined to 2.37-Å resolution per estimation by gold-standard Fourier shell correlation (GSFSC) threshold at 0.143 between two independent half-maps (Fig. 2, middle; Table 1; and fig. S1) (14). Cryo-EM and crystal structures of Pol γ ternary complexes were previously shown to be identical (11), thus comparison can be reliably carried out on structures determined using different techniques.

The catalytic subunit Pol γ A consists of Exo, spacer, and Pol domains. The Pol domain adopts a canonical right-hand configuration, with subdomains termed Thumb that binds to the upstream (–10 to –5 region) of primer/template DNA, Palm that houses the catalytic site, and Fingers that constitutes the incoming nucleotide binding site. The overall structure of the binary complex is similar to the ternary complex [root mean square deviation (RMSD) of 0.713 Å], except the following regions.

Opened Fingers

Relative to the dNTP-bound ternary complex, the Fingers subdomain of the binary complex rotates ~30° away from the catalytic center, adopting an “open” conformation (Fig. 3, A and C). If a dNTP was to bind to an open Fingers subdomain in the binary complex, then its α -phosphate (P α) would be 13.1 Å from the 3'-OH of the primer, a distance too long for phosphodiester bond formation. That distance in the ternary complex is shortened to 4.0 Å. The

open-closed Fingers conformational change is critical for the formation of a catalytically competent configuration, which has been observed in other high-fidelity DNA polymerases [see review (15)].

Pre-catalytic Pol active site

In the binary complex Pol site, Tyr⁹⁵⁵ protrudes into the N-site, and the templating nucleotide T_n is lifted from the coding-competent position, thus it is unable to form a base pair with the incoming nucleotide. The 3'-end of the primer in the binary complex is in the posttranslocated state in the P-site (Fig. 3A).

In the ternary complex, Arg⁸⁵³ and Gln¹¹⁰² are termed the “fidelity switch” (11) owing to H-bonding interactions with Watson-Crick paired T_n and incoming nucleotide as well as the nascent base pair. Arg⁸⁵³ also interacts with His¹¹³⁴ on the catalytic loop adjacent to the catalytic residue Asp¹¹³⁵ (Fig. 3B). All interactions are conserved in the binary complex (Fig. 3A), which holds Asp¹¹³⁵ in an identical position in the binary and ternary complexes (fig. S2A).

Crystal structure of Pol γ R853A ternary complex

To analyze the structural basis of reduced Pol activity and nucleotide binding stemming from Arg⁸⁵³ substitution, the ternary complex of the Pol γ mutant holoenzyme was formed with Pol γ A R853A *exo*[–]; Pol γ B Δ I4, a 24-nt/28-nt DNA; and a correct incoming nucleotide, dCTP (2'-deoxycytidine 5'-triphosphate). The complex was crystallized, and diffraction data were collected to 3.4-Å resolution. The structure was determined using molecular replacement using the WT ternary structure as a search model [Protein Data Bank (PDB): 4ZTZ]. The structure was refined to $R_{\text{work}}/R_{\text{free}} = 0.27/0.28$ (Table 2).

Unusual correct nucleotide binding

Although crystals of the Pol γ R853A ternary complex were formed in the presence of the correct incoming nucleotide, dCTP, the binding mode of dCTP differs from that of the WT ternary complex. In the WT Pol γ ternary complex, dCTP is bound in the N-site by

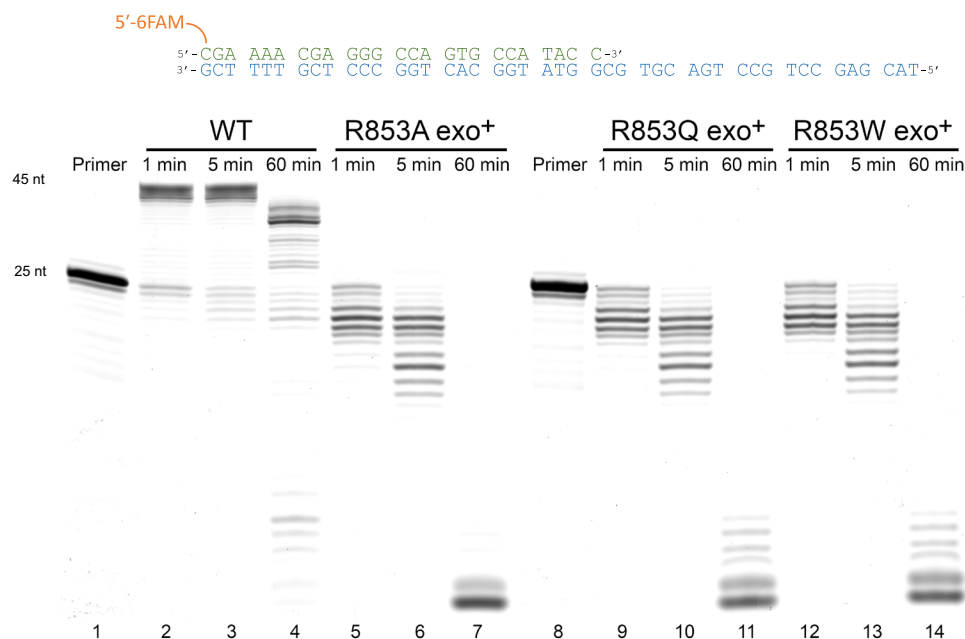


Fig. 1. Comparison of polymerase activity between wild-type Pol γ and R853 mutants. Polymerase activity of WT Pol γ (lanes 2 to 4), Pol γ R853A (lanes 5 to 7), Pol γ R853Q (lanes 9 to 11), and Pol γ R853W (lanes 12 to 14) were assayed on 5'-6FAM–25-nt primer (lanes 1 and 8) annealed to 45-nt template at 5, 10, and 60 min.

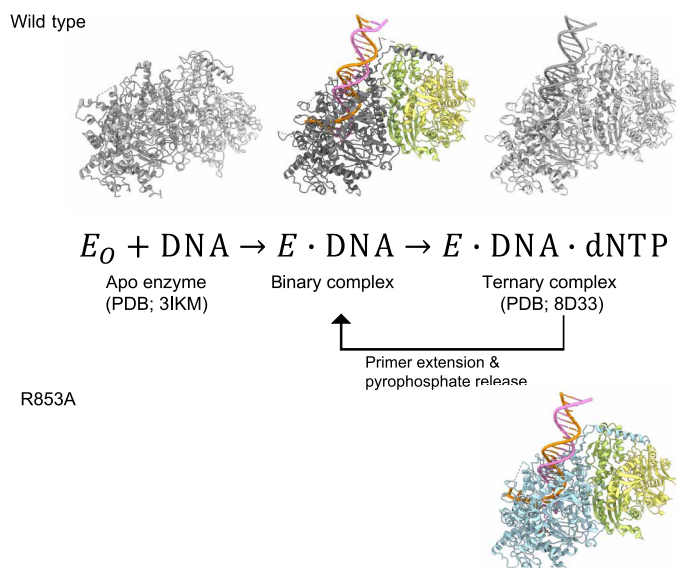


Fig. 2. Schematics of nucleotide incorporation cycle with representative Pol γ structures.

displacing Tyr⁹⁵⁵ and forming base-pairing interaction with the templating base dG_n; Arg⁸⁵³ forms an H bond between its N_η⁺ and the ribose O4' of the dCTP (Fig. 3B). In the mutant Pol γ ternary complex, the nucleobase does not form Watson-Crick base pair with the templating dG_n, instead is rotated ~90°, translated 13.2 Å, and bound in a pocket enclosed by Asp¹¹⁹², Asp¹¹⁸⁴, and Asp⁸⁹⁰, while the triphosphate moiety remains bound to the Fingers domain through charge interactions with Arg⁹⁴³ and Lys⁹⁴⁷ (Figs. 3D and 4D and fig. S3). The N-site is still occupied by Tyr⁹⁵⁵, and the templating residue T_n is precluded from the N-site (Fig. 3D), adopting a configuration nearly identical to the binary complex in the absence of an incoming nucleotide (Fig. 3E).

Opened Fingers

Different from the WT ternary complex, the correct dCTP binding did not induce the closing of the Fingers; instead, the Fingers subdomain remains in an open conformation that closely resembles the WT binary complex (Figs. 3, D and E, and 4, A and D); the RMSD of the mutant to the binary complex is 1.435 Å and the ternary complex is 2.248 Å. However, the Fingers subdomain of R853A is slightly less open than the binary complex, with the Fingers subdomain rotated 1.56° toward the active site.

Catalytically incompetent Pol site

The loop harboring the catalytic residue Asp¹¹³⁵ in the mutant Pol site undergoes a 1.5-Å displacement away from its catalytic competent position (fig. S2B). This misaligned catalytic residue resembles that of the apo enzyme and could, in part, account for the reduced Pol activity (fig. S2C).

Arg⁸⁵³ forms a multivalent interaction network with the incoming nucleotide dNTP and nascent base pair. R853A mutation could reduce the affinity of the enzyme to dNTP and subsequently fail to induce Fingers' conformational change necessary for catalysis, both contributing to the lack of DNA synthesis activity in Pol γ R853X mutants.

Structural basis for the diseases mutant R853Q and R853W

To understand the disease phenotype of R853Q and R853W, we substituted Ala⁸⁵³ in the ternary complex with Gln and Trp, respectively,

in silico, with minimal clashes with surrounding residues. The operation shows that R853Q substitution extends the distance between its ε-NH₂ to ribose's O4' of the dCTP to 6.4 Å, more than double the distance of an H bond (Fig. 4C); R853W substitution resulted in a hydrophobic side chain, whose bulky indole could prevent closing of the Fingers domain independently and the N7 of the indole is 7.6 Å from the O4' of the dCTP (Fig. 4F). Thus, R853Q and R853W substitutions share the same defects as the R853A, where the H-bonding network coordinated by R853 with the dNTP and with the catalytic triad are abolished.

Incoming nucleotide binding affinity

To independently verify the structural conclusion that Arg⁸⁵³ substitution reduced dNTP binding affinity, we used isothermal titration calorimetry (ITC) to measure a correct incoming nucleotide (dCTP) binding to Pol γ WT *exo*⁻ and R853A *exo*⁻ (Fig. 5). The dCTP was titrated into a preformed binary complex of Pol γ and 25-nt/45-nt DNA up to 200 μM and 2 mM for WT (Fig. 5A) and R853A (Fig. 5B), respectively. The measured dissociation constants (*K_d*) were 55 nM for WT and 37 μM for R853A, which correspond to Δ*G* = -10.329 for WT and -6.298 kcal/mol for R853A, indicating that the lack of Arg⁸⁵³ resulted in ~4 kcal/mol binding energy reduction and a 670-fold lower binding affinity.

Global and domain motion changes revealed by molecular simulations

As the biochemical and structural analyses revealed an imbalance in Pol and Exo activities and the lack of necessary conformational changes in the R853A mutant, we evaluated the difference between the mutant and WT Pol γ using MD simulations. Note that the initial point of the simulation of the two structures is the same, namely, the WT Pol γ closed, ternary complex (PDB: 4ZTZ) except for the substitution at residue 853 for the mutant system. During the visualization of the simulation, we noticed that the regions modeled by Rosetta exhibited high flexibility, thus increasing the overall average RMSD of the system, but the domains present in the crystal structures were unaffected. Therefore, the analyses only included specific subdomains on Pol γ A (Palm, Fingers, and Thumb) present in the crystal structure and excluded the homology-modeled region. The calculations have been carried out in triplicate, the results for all three replicates for each system are similar, and thus, the first replicate has been chosen as representative for the discussion below.

The average RMSD for the DNA bound to the mutant is notably higher than that to WT, and the mutant's Thumb, Fingers, and Palm subdomains also exhibit increased RMSD in the mutant compared with the WT, albeit at lower values (Fig. 6, B and C; tan, blue, and pink lines, respectively), indicating a deviation from the WT structure. The primer/template in the mutant exhibited the largest deviation from the WT (Fig. 6, B and C; green and purple lines), suggesting that the mutation affects the configuration of the bound DNA. Similarly, the average root mean squared fluctuation (RMSF) shows that the above subdomains exhibit larger fluctuations in the mutant than in the WT (Fig. 6D). The average RMSF of the Exo domain was observed to be higher in the WT than in the mutant.

A dynamic cross-correlation analysis was done to investigate the effect of the mutation on the correlated motion of the systems (fig. S4). Difference plots between the mutant and the WT, with the WT as a reference, show several changes in correlated movement between the domains of the polymerase for the two systems

Pol γ binary complex	
Data collection and processing	
Magnification	105,000
Voltage (kV)	300
Electron exposure (e ⁻ /Å ²)	50
Defocus range (μm)	−1.5—2.5
Pixel size (Å)	0.425
Symmetry imposed	C1
Number of micrographs	
Collected	8,012
Used	7,137
Initial particle images (no.)	10,947,987
Final particle images (no.)	6,773,711
Map resolution (Å)	
Corrected, FSC = 0.143	2.37
Refinement	
Initial model used (PDB code)	8D33
Model resolution (Å)	2.6
FSC threshold	0.5
Map sharpening <i>B</i> factor (Å ²)	
Model composition	
Non-hydrogen atoms	14,676
Protein/DNA residues	1,785/46
<i>B</i> factors (Å ²)	
Protein	36.34
DNA	41.18
RMSD	
Bond lengths (Å)	0.003
Bond angles (°)	0.738
Validation	
MolProbity score	1.12
Clash score	1.27
Poor rotamers (%)	0.19
Cβ outliers (%)	0.00
Ramachandran plot	
Favored (%)	96.02
Allowed (%)	3.92
Disallowed (%)	0.06
<i>Q</i> -score	
Protein	0.668
DNA	0.646

(fig. S4A). Most notably, the Fingers subdomain of the polymerase shows an increased anticorrelated movement with the Thumb and Palm subdomains in the WT system as compared to the mutant (fig. S4B). This indicates that the residues in the Fingers subdomain move in an opposite direction to that of the Thumb and Palm subdomains in the WT, indicating the possibility of an opening and closing motion of the polymerase in the WT, while this motion is not observed in the mutant system. The Exo domain and the

Fingers subdomain show an increased correlation in the mutant as compared to the WT. As the Exo domain remains static during the reactions, the results suggest a reduced likelihood for the Fingers subdomain to undergo the closing conformational change. The essential dynamics of the domains are better illustrated by the normal mode analysis (NMA) (fig. S5). The top 10 modes among the 100 modes calculated were considered. Two types of motion were seen to be the primary contributors to the dynamics of the

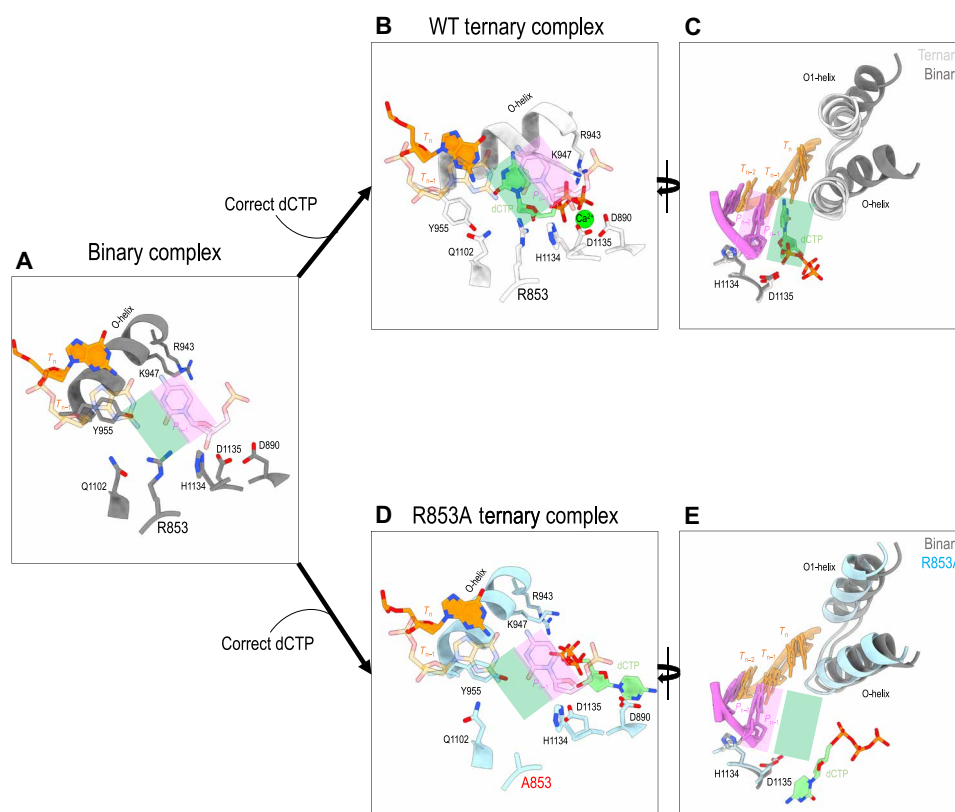


Fig. 3. Structural comparison of wild-type Pol γ ternary and binary complexes with Pol γ R853A ternary complex. (A) Pol site of WT Pol γ binary complex. (B) Pol site of WT ternary complex. (C) Superposition of WT Pol γ binary and ternary complexes. (D) Pol site of Pol γ R853A ternary complex. (E) Superposition of WT binary and Pol γ R853A ternary complexes.

systems: breathing and rocking (movie S1). The primary contributor for the WT system, mode 1 (around >95%) corresponds to a breathing-like motion with most changes observed on the Thumb, Fingers, and Palm subdomains, while the second mode (<5% contribution to overall motion) corresponds to a rocking motion (fig. S5, A, C, and E to G; and movie S1). Conversely, for the mutant system, the first mode corresponds to the rocking motion and represents about 60 to 70% of the overall contribution to the motion, and mode 2 has a much higher contribution, around 20 to 40% in the mutant, and corresponds to a breathing motion (fig. S5, B, D, and H to J; and movie S1). It is interesting to note that the contributors to the motion are inverted from the WT to the mutant. The breathing motion of the WT is also consistent with the dynamic cross-correlation difference analysis in the previous section, where it was seen that, in the WT, the Fingers show anticorrelated movement with the Thumb and Palm subdomains, suggesting an opening and closing movement of the system in the WT, similar to a breathing motion, which is not the dominant movement in the mutant. These results suggest that the WT system exhibits dynamic motion that is consistent with Pol activity since the breathing motion corresponds to the natural open-to-close motion observed for the binary to ternary transition. On the other hand, the mutation changes the dynamics of the system to a more rigid rocking motion, markedly reducing the contribution from the breathing motion, which suggests an inhibition of the motion of the polymerase, hence causing a disruption to the catalysis.

Indication of catalytic incompetent Pol site in R853A by MD simulation

We sought to map the R853A substitution-induced changes in the Pol site using MD simulations (Fig. 6, E to G). We initially focused on four key distances: (i) Primer O3' to dCTP P α (tan), (ii) Primer O3' to Mg $_A^{2+}$ (purple), (iii) Asp 1135 OD $_8$ to Mg $_A^{2+}$ (green and pink), and (iv) Asp 890 OD $_8$ to Mg $_B^{2+}$ (blue). The main difference in distance was between the Primer O3' and the dCTP P α , which extends from 3.5 Å in the WT to 4.3 Å in the R853A mutant (Fig. 6, F and G; tan line).

A clustering analysis using the *k*-means algorithm was performed, considering all calculated structures (combined trajectories = 150,000 snapshots; see the Supplementary Materials for clustering based on individual replicates). Distances of the Primer O3' to the dCTP P α (d1) were plotted against that of the Primer O3' to Asp 1135 (d2) for WT and R853A mutant (Fig. 6, H and I). In the WT, 40% of the snapshots corresponding to three clusters are within d1 = {3.0 to 3.8 Å} and d2 = {2.8 to 3.5 Å} (Fig. 6H), whereas less than 15% of the snapshots in the mutant (corresponding to only one cluster) were located in the same area (Fig. 6I). Moreover, most of the snapshots in the R853A mutant structure are clustered at longer d1 and d2 distances, which is consistent with an open Fingers position resulting in an extended distance between the reactants for DNA synthesis.

A superposition of WT crystal structure (PDB: 4ZTZ) (fig. S6A, green) and a representative of the WT simulation (fig. S6A, gold) show high similarity (fig. S6A), whereas R853A simulations (fig. S6B, pink)

Table 2. Crystal structure refinement statistics of Pol I^γ R853a ternary complex.

Pol γ R853A ternary complex	
Data collection	
Wavelength (Å)	0.979
Space group	P4 ₁ 2 ₁ 2
Cell dimensions	
<i>a</i> , <i>b</i> , <i>c</i> (Å)	215.41, 215.41, 169.97
α, β, γ (°)	90, 90, 90
Resolution (Å)	48.84–3.435 (3.557–3.435)*
<i>I</i> / <i>σ</i> <i>I</i>	
Completeness (%)	98.17 (93.98)
Refinement	
Resolution (Å)	
Unique reflections	52,823 (4,968)
<i>R</i> _{work} / <i>R</i> _{free}	0.196/0.234
No. of atoms	14,330
Macromolecules	14,302
Ligand	28
RMSD	
Bond lengths (Å)	0.004
Bond angles (°)	0.61
Ramachandran	
Favored (%)	96.56
Allowed (%)	3.38
Outliers (%)	0.06
Rotamer outliers (%)	0.00
Clash score	5.03
Average <i>B</i> factors	129.73
Macromolecules	126.59
Ligands	219.06

*Statistics for the highest resolution shell are shown in parentheses.

shows that the substitution resulted in an open Fingers and Thumb configuration that are deviated from the WT crystal structure (fig. S6), with the RMSD values for the Thumb and Fingers between the crystal structure and the mutant MD representative at 7 and 4 Å, respectively. Together, these results show that the MD simulations reproduce the observed experimental structural features and provide further insights into the major impact of the R853A mutation on the structure of Pol γ.

We next analyzed residues involved in stabilizing or destabilizing dCTP (fig. S7A) and the mutation site at Arg⁸⁵³ (fig. S7B) using energy decomposition analysis (EDA). Residues with the largest energetic contribution are listed (fig. S7C). Arg⁸⁵³ provides the largest, 123.8 kcal/mol, stabilization energy to dCTP in the WT, whereas Lys¹¹⁹¹ is the largest contributor 125.0 kcal/mol to dCTP in mutant Ala⁸⁵³ structure (fig. S7, A and C). Arg⁸⁵³ mutually stabilizes Asp⁸⁹⁰, Glu⁸⁹⁵, His¹¹³⁴, Asp¹¹³⁵, and Glu¹¹³⁶, forming an interaction network. Substitution of Arg to Ala loses 123 kcal/mol stabilization energy, which is compensated by energetics from Arg⁸⁶⁶, Asp⁸⁹⁰, Arg⁹⁴³, Lys⁹⁴⁷, Lys¹¹⁹¹, and Glu¹¹³⁶. The computational results are in good agreement with the mutant ternary structure where the nucleobase

of dCTP binds to a pocket of Asp⁸⁹⁰, Lys¹¹⁹¹, and Glu¹¹⁹², while the triphosphate is bound to Arg⁹⁴³ and Lys⁹⁴⁷. To account for the 50,000 structures used in each replicate, the EDA of representative replicates of both WT and mutant systems have been presented with error bars, as separated Coulomb and van der Waals interactions, with mutation site Arg/Ala⁸⁵³ as the reference residue (fig. S8). The small error bars show that the interactions between the residues remain mostly similar throughout the simulation.

DISCUSSION

Mitochondrial genome integrity is essential for the organelle functions. Mutations on mtDNA are associated with multi-system disorders. We investigated Pol γ Arg⁸⁵³ mutations (R853Q and R853W) that are implicated in severe clinical disorders (8, 9). Although not a catalytic residue, substitutions of Pol γ Arg⁸⁵³ are completely void of polymerase activity. Our studies revealed that Pol γ achieves high fidelity by a balanced energy partition for the moieties of a correct nucleotide, which could be generalized to other A-family DNA polymerases due to their shared structural features.

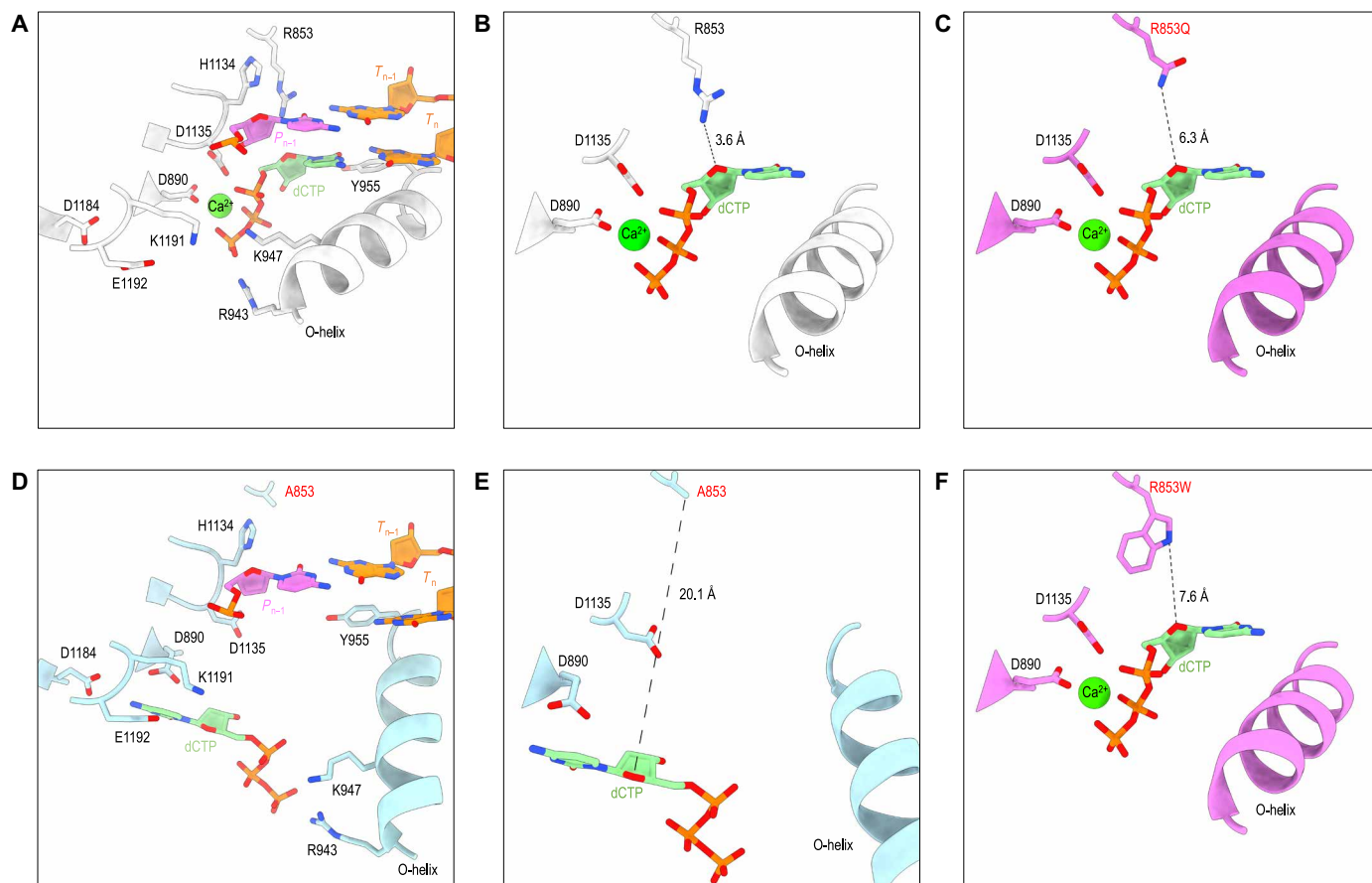


Fig. 4. Comparison of dCTP binding between Pol γ wild type and R853A ternary complexes. Polymerase active site of WT Pol γ ternary complex (A) and of Pol γ R853A (D) ternary complexes. Distance between Arg⁸⁵³/Ala⁸⁵³ to O4' of dCTP is shown for WT Pol γ ternary complex (B) and of Pol γ R853A (E) ternary complexes. Substitutions R853Q (C) and R853W (F) were made in the Pol γ R853A ternary structure in silico with a minimal clash with surrounding residues in UCSF ChimeraX. The Gln⁸⁵³ δ NH is 6.4 Å from the O4' of the dCTP (C). The indole ring of Trp⁸⁵³ is unable to form an H bond with the O4' of the dCTP and its bulky hydrophobic side chain could independently prevent the closing of the Fingers' domain (F).

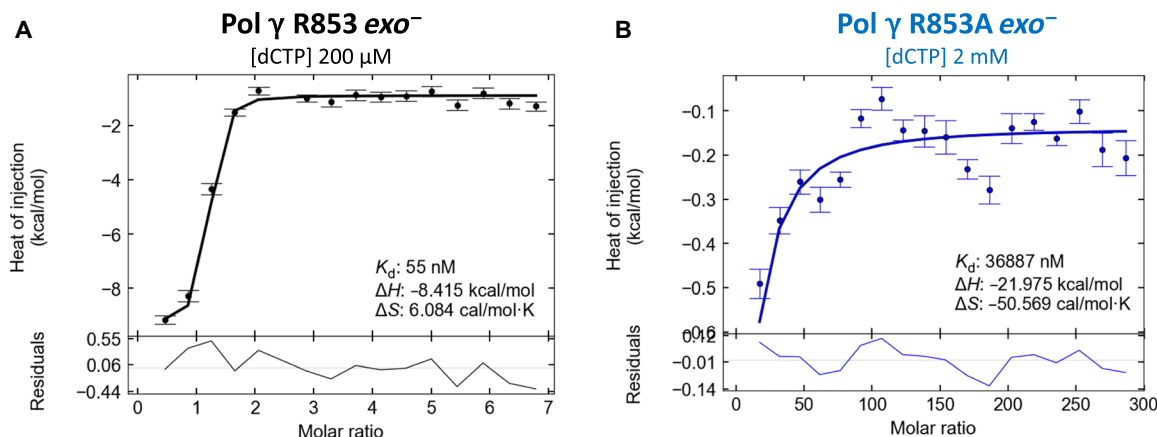


Fig. 5. Isothermal calorimetry data of correct incoming nucleotide binding in Pol γ . ITC graphs of WT Pol γ (A) and Pol γ R853A mutant (B) binary complexes binding to dCTP.

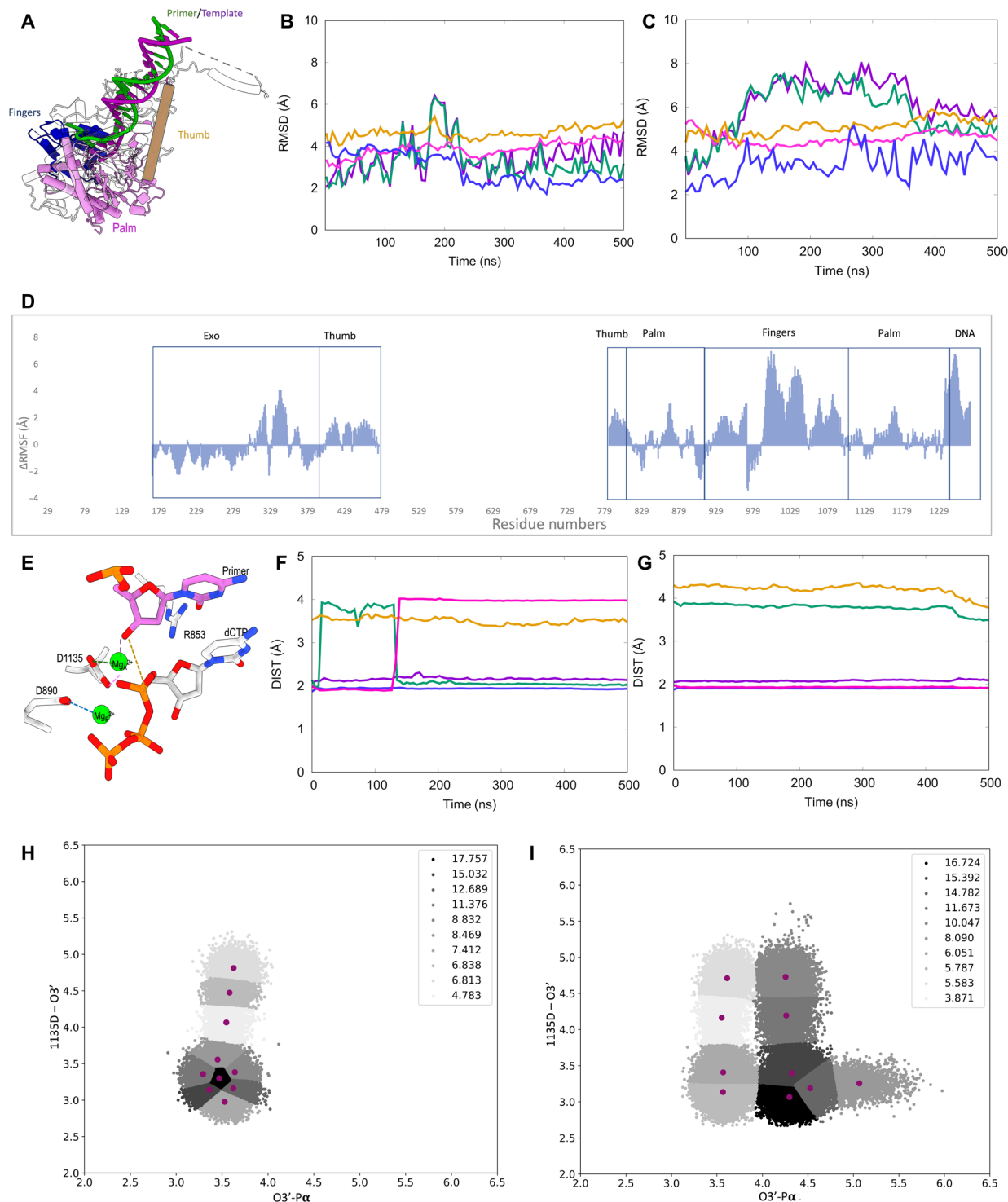


Fig. 6. Molecular dynamics simulation of wild-type Pol γ and Pol γ R853A ternary complexes. (A) Structural subdomains of Pol γ A: pink, Palm; tan, Thumb; blue, Fingers; green/purple, DNA primer/template. RMSD per subdomain for WT Pol γ (B) and Pol γ R853A mutant (C) following the color scheme in (A). (D) Difference between the average values of RMSF between Pol γ R853A mutant and WT pol γ (Mut-WT). (E) Polymerase active site with representative catalytic distances denoted by dashed lines. Color key: purple, Mg_A^{+2} and O3' of DNA primer; tan, O3' and α -phosphate of dCTP; green, OD2 of Asp¹¹³⁵ and Mg_A^{+2} ; pink, OD1 of Asp¹¹³⁵ and Mg_A^{+2} ; blue, Asp⁸⁹⁰ and Mg_A^{+2} . Distance analysis of the WT Pol γ (F) and the Pol γ R853A mutant (G) for the catalytic residues in the polymerase active site following the color scheme in (E). k -means clustering analysis for the WT Pol γ (H) and Pol γ R853A (I) based on the O3'- α -phosphate (x axis) and the Asp¹¹³⁵-O3' (y axis) distances. Replicas of these calculations are presented in fig. S9 (A to F).

Modular energetics of dNTP binding

To maintain high replication fidelity, a DNA polymerase should not only select a correct nucleotide from the pool deoxy- and ribo-nucleotides but also recognize chemical modifications to its nucleobase, deoxyribose, and triphosphate moieties. A high-fidelity DNA polymerase uses checkpoints for selection of the correct nucleobase via Watson-Crick base pairing, as well as base-shape complementarity because even modified nucleotides without H bonding also can be incorporated (16), albeit at much lower efficiency; selection of the deoxyribose moiety against ribose is accomplished by a “steric gate” tyrosine (17, 18), and selection of the triphosphate moiety is likely done by its configuration (19). Proof-reading of misincorporation in the Exo site further increases the replication fidelity (16, 20, 21).

In this study, we identified Arg⁸⁵³ in Pol γ binds to the deoxyribose of dNTPs. Substitutions of Arg⁸⁵³ (R853Q/W/A), conserved among A-family DNA polymerases, eliminate this interaction, markedly reducing dNTP binding affinity. We noticed that the ~10 kcal/mol of free enzyme for Pol γ binding to a correct nucleotide is contributed modularly by the interaction with dNTP moieties: the electrostatic interaction with triphosphate at the initial binding contributes 4 to 5 kcal/mol (22), and Watson-Crick base pairing contributes ~0.3 kcal/mol free energy ($\Delta\Delta G$) between correct and incorrect nucleobases (23). The energetic discrepancy suggests additional contributors to dNTP binding energy. In this study, we identified that Pol γ Arg⁸⁵³ forms an H bond with the ribose moiety of the incoming nucleotide, the measured ΔG difference between WT and R853A mutant for dCTP binding is 4 kcal/mol, or about 40% of total dNTP binding, which is greater than a single hydrogen bond, showing additional energetic contribution of the Arg⁸⁵³ beyond interaction with the ribose. Nevertheless, the ribose interaction enables the polymerase to distinguish deoxyribose from other pentocyclic analogs, such as cyclopentane, thiophene, or selenophene.

Despite the moieties contributing unequally to the free energy to enzyme binding to dNTP, missing any of the components will prevent dNTP incorporation and halt the polymerase DNA synthesis. The formation of Watson-Crick base complementarity is essential

but additional interaction with the ribose and phosphate moieties is sufficient for a correct nucleotide incorporation by Pol γ . Only when all moiety checkpoints are satisfied does the polymerase incorporate the dNTP. The modular dNTP recognition is not only critical to mtDNA replication fidelity but also important for Pol γ exclusion of nucleotide/nucleoside antiviral drugs and reducing drug toxicity.

The central role of Arg⁸⁵³ in the catalytic interaction network in the Pol site

Our structural studies revealed an interaction network in Pol γ Pol site centered at Arg⁸⁵³ that stabilizes the two reactants of phosphoryl transfer reaction, the 3'-end of the primer DNA and dNTP and coordinates the catalytic residue Asp¹¹³⁵ via His¹¹³⁴. The Arg-His-Asp residues are highly conserved both in sequence and in structure among members of A-family DNA polymerases that include *Escherichia coli* DNA Pol I, T7 DNA Pol, and most mtDNA polymerases (Fig. 7).

Mutation studies of the Pol I equivalent Arg⁶⁶⁸-His⁸⁸¹-Asp⁸⁸² residues revealed their contribution to the enzyme kinetics: Arg⁶⁶⁸ mutation reduced the catalytic proficiency by 1300-fold with both increased K_m and reduced k_{cat} , whereas mutations on Asp⁸⁸² or His⁸⁸¹ only reduced the k_{cat} by ~400- and 10-fold, respectively. Consequently, the Arg⁶⁶⁸ mutant reduced the catalytic proficiency more than the catalytic residue Asp⁸⁸² (24–26). The kinetic studies are in good agreement with structural and functional studies of Pol γ where Arg⁸⁵³ mutations resulted in an open, catalytically incompetent configuration upon binding to a correct dNTP with shifted catalytic loop. The importance of Arg in the coordination of the 3'-end of the primer and dNTP was also tested in DNA Pol I. When substrate dNTP was substituted with dUTP, where the O4' of the ribose was replaced with a C4' and the H bond between Arg⁶⁶⁸ with the ribose would be obliterated, the k_{pol} was reduced by 1600-fold, similar to the magnitude of reduction in abolishing the H bond between Arg⁶⁶⁸ and 3'-OH of the primer (27).

MD simulations for the Pol γ R853A revealed two major impacts of the in silico mutation: (i) elongated distance between the 3'-OH of primer DNA and P α of dCTP and (ii) higher flexibility of the Fingers subdomain relative to other subdomains. The changes are

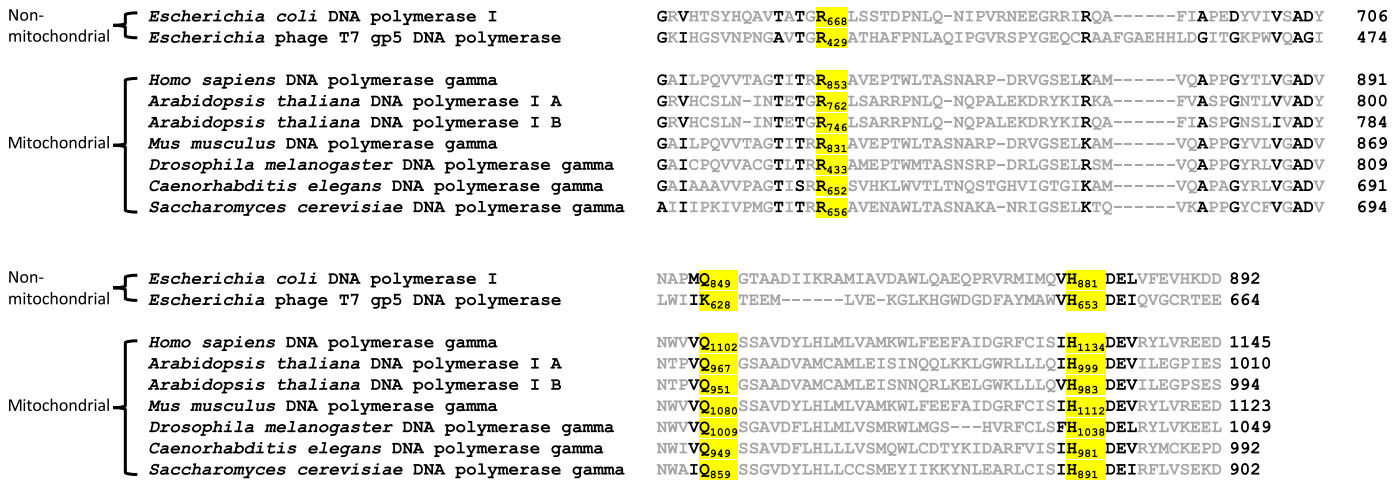


Fig. 7. Sequence alignment of replicative A-family DNA polymerases. Sequence alignment of Pol γ with other non-mitochondrial (top) and mitochondrial (bottom) A-family DNA polymerases. Highly conserved amino acids are shown in black, and the “fidelity switch” (Arg⁸⁵³, Gln¹¹⁰², and His¹¹³⁴ in Pol γ) has been highlighted in yellow.

consistent with the noncanonical binding of dCTP to open the Fingers subdomain in Pol γ R853A crystal structure. Such abnormal dCTP binding mode loses Watson-Crick base pair interaction and is seen interacting with a protein pocket, which is in excellent agreement with EDA analysis showing that the same residues selectively stabilize R853A substitution. Considering MD simulations for the Pol γ R853A variant started from a catalytically competent, closed WT ternary conformation, the results revealed intrinsic functions of Arg⁸⁵³ that deviate from the starting WT structure, providing strong independent support to the experimental R853A ternary complex structure.

Altered enzyme dynamics by Arg⁸⁵³ mutation

MD simulation and NMA indicate that Pol γ R853A displays dynamic changes from the WT. While wild-type motion is predominantly in a “breathing” mode, which likely is a movement necessary for proper catalysis, a smaller population (20 to 40%) of Pol γ R853A adopts such mode, suggesting that catalytically competent movement (closing of the Fingers) is still possible albeit less efficient. The *k*-means clustering analysis supports such an idea, as Pol γ R853A shows a bimodal distribution: while a large population is catalytically incompetent ($d1 > 4.0$ Å), a small fraction of them maintains the catalytically competent distance ($d1 < 3.8$ Å), similarly to that of the WT. However, as evident by studies in this work and those in the literature, correct configuration alone is insufficient for catalysis, and the presence of Arg⁸⁵³ in Pol γ is an absolute necessity.

We noticed that the distance between the C β of Ala⁸⁵³ and O4' of dCTP in the Pol γ mutant ternary complex crystal structure is longer than that in the MD simulation. The observation, together with increased dynamics induced by the mutation, suggests that the crystal structure likely represents one conformation in a dynamic ensemble of populations. Probing the mutational effect on Pol γ dynamics warrants further investigation.

MATERIALS AND METHODS

Protein expression and purification

Proteins were prepared as previously described (13). Briefly, Pol γ A WT, Exo-deficient [D198A/E200A (*exo*[−])], and mutants [Pol γ A R853A, Pol γ A R853Q, Pol γ A R853W, and Pol γ A R853A (*exo*[−])] were expressed in insect cells Sf9 and purified using TALON (Clontech) and Superdex 200 (Cytiva) column chromatography. Pol γ B WT and a deletion mutant Pol γ B- Δ I4 (deletion of amino acids 136 to 182) were expressed in *E. coli* Rosetta BL21 DE3 and purified using Nickel-NTA (Qiagen) and cation-exchange (Mono S) chromatography. For structural studies, purified Pol γ A and Pol γ B were mixed at a 1:2 molar ratio on ice for 10 min and purified using Superdex 200 (Cytiva) column chromatography. The protein purity was estimated to be >95% per SDS–polyacrylamide gel electrophoresis analysis.

Oligonucleotide substrates

For activity assays, a 25-nt primer (5'-CGA AAA CGA GGG CCA GTG CCA TAC C-3') with 5'-6FAM modification and a 45-nt template (5'-TAC GAG CCT GCC TGA CGT GCG GTA TGG CAC TGG CCC TCG TTT TCG-3') were synthesized by Integrated DNA Technologies. Primer and template were annealed at a 1:1 ratio in buffer [20 mM Tris (pH 8.0), 100 mM NaCl, and 1 mM EDTA (pH 8.0)] by heating the mixture to 95°C for 5 min, followed by slow cooling to room temperature overnight.

High-performance liquid chromatography–purified 24-nt primer (5'-CGA AAA CGA CGG CCA GTG CCA TAC-3') and 28-nt template (5'-CGA GGT ATG GCA CTG GCC GTC GTT TTC G-3') were synthesized and annealed as described above for crystallographic and cryo-EM studies. For crystallization, dC at the 3'-end of the 24-nt primer was replaced with ddC to prevent any enzymatic reaction.

Polymerase activity assays

A total of 400 nM Pol γ and 400 nM duplex DNA were mixed on ice in reaction buffer [25 mM Hepes (pH 7.5), 140 mM KCl, 5% glycerol, 1 mM EDTA (pH 8.0), and BSA (100 μ g/ml)] and prewarmed at 37°C for 5 min. Reactions were initiated by adding an equal volume of reaction buffer containing 20 mM MgCl₂ and 100 μ M dNTP. Final concentrations were 200 nM for Poly-DNA complex, 10 mM for MgCl₂, and 50 μ M for dNTP. Reactions were incubated at 37°C for the indicated time and stopped by adding the fourfold excess volume of quench buffer [80% formamide, 50 mM EDTA, 0.1% (w/v) SDS, 5% glycerol, and 0.02% bromophenol blue]. Reaction products were denatured by heating at 95°C for 5 min, resolved on a 20% polyacrylamide denaturing (7 M Urea) gel electrophoresis, and imaged using an Amersham Typhoon Biomolecular Imager (Cytiva).

Isothermal titration calorimetry

Pol γ WT *exo*[−] and R853A *exo*[−] were dialyzed against Buffer RX [25 mM Hepes (pH 7.5), 140 mM KCl, 10 mM CaCl₂, 5% glycerol, and 1 mM β -mercaptoethanol (BME)] at 4°C overnight. dCTP was diluted from a 100 mM stock to the indicated concentration. Following dialysis, protein concentration was determined using the extinction coefficient $\epsilon_{280} = 3.86 \times 10^5 \text{ M}^{-1} \text{ cm}^{-1}$ for the heterotrimer. Pol γ :DNA complexes were made by incubating protein and DNA at a 1:1 ratio (5 μ M:5 μ M) at room temperature for 10 min. Titrations were carried out using a Malvern MicroCal PEAQ-ITC at 37°C with 19 injections (0.4 μ l for the first injection, followed by 18 injections of 2 μ l) of 200 μ M or 2 mM dCTP titrated into 5 μ M protein:DNA complex. Control titrations were performed by titrating 200 μ M or 2 mM dCTP into the buffer. Thermodynamic binding parameters were determined using NITPIC and SEDPHAT as described in (28).

Crystal structure determination of Pol γ R853A ternary complex

Crystallization

For crystallization, 63.5 μ M complex Pol γ A R853A (*exo*[−])/Pol γ B Δ I4 was mixed with 114.3 μ M 24-nt/28-nt DNA in the presence of 10 mM CaCl₂ and 2 mM dCTP and subjected to crystallization after incubation on ice for 10 min. Crystals were formed using the hanging-drop vapor diffusion method at 20°C against the well solution [100 mM MES (pH 6.0), 150 mM NaCl, 10 mM CaCl₂, 50 mM BME, 3% PEG-8000 (polyethylene glycol, molecular weight 8000), 1 to 8% sucrose, 2% Jeffamine, and 0.8 M nondetergent sulfobetaine (NDSB)]. Crystals were cryoprotected in solutions containing 30% glycerol, 30% 2-Methyl-2,4-pentanediol (MPD), 25 mM BME, and 1 mM dCTP and flash-frozen.

Data collection, processing, and refinement

Diffraction data were collected from a single crystal at beamline 5.3 Advanced Light Source (ALS, Berkeley Laboratory) using wavelength 1.0-Å x-ray, recorded on a charge-coupled device detector. The crystals exhibited a tetragonal space group, P4₁22, with cell

dimensions $a = 215.41$, $b = 215.41$, and $c = 169.97$. Data were processed with HKL3000 (29). The structure was determined using molecular replacement using a WT Pol γ ternary complex (12) as the search model. The Fingers movement in the mutant structure was clearly valuable in the Fo-Fc map and was manually built into 2Fo-Fc and Fo-Fc maps using Coot (30). The structure was refined using PHENIX (31).

Cryo-EM structural determination of wild-type Pol γ binary complex

Sample preparation

WT Pol γ (2 μM) was mixed with 2 μM DNA and incubated on ice in a buffer containing 20 mM Hepes (pH 7.5), 140 mM KCl, 1 mM EDTA (pH 8.0), 10 mM CaCl_2 , 10 mM BME, and 0.01% (w/v) octyl- β -glucoside. A frozen grid was prepared by applying 4 μl of the sample on a plasma-cleaned QUANTIFOIL R 2/1 Cu 200 grid (Electron Microscopy Sciences) using Vitrobot Mark IV at 22°C and 100% humidity (Thermo Fisher Scientific).

Data collection

Frozen grids of Pol γ binary complex were loaded into a Titan Krios G3i (Thermo Fisher Scientific) equipped with K3 direct electron detector with BioQuantum energy filter (15-eV energy slit) (Gatan) and operating at 300 keV at Stanford SLAC Cryo-EM Center. Cryo-EM data were automatically acquired using EPU software in counted super-resolution mode at a nominal magnification of $\times 105,000$ (corresponds to 0.43 Å/pix) with a nominal defocus range between -1.5 and -2.5 μm . Forty-frame movie stacks were collected over 2-s exposure with a total dose of 49.6 $\text{e}^-/\text{\AA}$. A total of 8012 movie data were collected.

Structural determination

The movie frames were imported into cryoSPARC (32) for image processing (fig. S1A). Movies were motion-corrected and $2\times$ binned using Patch Motion Correction. Contrast transfer function (CTF) of resulting micrographs was determined using patch CTF estimation. After preprocessing and discarding micrographs with CTF fit higher than 4 Å and a total motion less than 50 pixels, 10,947,987 particles were picked from the resulting 7137 micrographs using Blob Picker. Particles were extracted with $4\times$ binning (80 pixels) and subjected to two iterative rounds of 2D classifications. A total of 200,000 particles out of the cleaned 6,773,711 particles were used in the Ab Initio building of three initial volumes. All particles were subjected to heterogeneous refinement using three volumes from Ab Initio (classes 1, 2, and 3). Then, 3,342,218 particles belonging to class 1 were subjected to another round of heterogeneous refinement using identical input volumes. A total of 2,732,032 particles in class 1 from the second heterogeneous refinement were recentered and re-extracted without binning (320 pixels), resulting in 2,504,778 particles. Homogeneous refinement of 2,504,778 particles resulted in 2.47 Å. Particles were further separated on the basis of conformational heterogeneity by running another round of heterogeneous refinement with three repeated input volumes resulting from the homogeneous refinement. Particles belonging to classes 1–1 and 1–3 were combined and further refined by homogeneous refinement followed by cryoSPARC's implementation of local and global CTF refinements (33) and a final round of non-uniform refinement (34), yielding 2.37-Å reconstruction according per GSFSC at 0.143 (fig. S1B). Local resolution of final reconstruction was estimated by cryoSPARC's implementation of blocres (35) and colored by resolution range from 2 to 4 Å in UCSF ChimeraX (fig. S1B) (36).

The cryo-EM map was postprocessed with LocSpiral (37). Cryo-EM structure of Pol γ -DNA-dCTP ternary complex (PDB ID: 8D33) (11) was rigid body fitting into LocSpiral-processed map using UCSF Chimera (38) and the unfitted regions were manually adjusted using Coot. The model was refined using real-space refinement in PHENIX (31), Coot (39), and ISOLDE (40). The refined model was validated by MolProbity (41) and Q-score analysis (42). Figures were prepared using UCSF Chimera (38) and UCSF ChimeraX (36).

Molecular dynamics simulations

Preparation of structural model for simulation

The crystal structure of mtDNA polymerase γ (4ZTZ) was used as the initial model. The missing regions were completed using homology modeling via RosettaFold (43). Twenty-five structures were built using Rosetta, and then they were compared to the crystal structure by overlaying the Rosetta structure with the crystal structure. Ten structures were selected from the best RosettaFold solutions and visually inspected. Each of the 10 structures was loaded onto visual molecular dynamics (44), and the RMSD with respect to the regions resolved in the crystal structure was calculated. The structure with the lowest overall RMSD (2.5 Å) was selected as our initial system. The mutated system was created by in silico introducing Arg⁸⁵³ to Ala substitution using Chimera UCSF (38).

MD simulation

The parameters for the incoming nucleotide in the Pol γ WT and R853A ternary complexes were set as previously reported (45). The protonation states were determined using ProPKA (46) and hydrogens were added to amino acids using MolProbity (41). The LeAP (47) module of AMBER18 was used to neutralize and solvate the system. The AMBER ff14SB (48) and gaff (49) forcefields were used for the protein and OL15 (50) for the DNA. The system was neutralized using 29 Mg^{+2} ions and the system was solvated using the TIP3P water model in a cubic box with a minimum of 12 Å between the edge of the protein and the box. Then, the volume of the system was noted, and 73 Mg^{2+} and 146 Cl^- ions were calculated to make the system into a 20 mM solution of MgCl_2 . Once the number of ions was determined, they were added at random to the system. The final system has 239,364 atoms for the WT and 236,912 atoms for the mutant.

The MD simulations were run using AMBER18 pmemd.cuda (51). Minimization was performed for a total of 10,000 cycles, with 5000 cycles using the steepest descent algorithm and the other 5000 cycles using the conjugated gradient algorithm followed by heating to 300 K using Langevin dynamics (52) with a collision frequency of 2 ps^{-1} . During this process, all heavy atoms were restrained with a force of 100 $\text{kcal mol}^{-1} \text{\AA}^{-2}$. Subsequently, the restraints were reduced gradually (table S1).

After the release of restraints, it was observed that some distortion occurred around the active site; therefore, selected residues in the Pol site, namely, the incoming nucleotide, Asp⁸⁹⁰ and Asp¹¹³⁵, Mg_A^{2+} and Mg_B^{2+} , and the primer 3'-OH terminus were restrained with a 0.5 $\text{kcal mol}^{-1} \text{\AA}^{-2}$ force for an additional 25 ns. The restraint was removed after 25 ns and the remainder of the simulations were run without restraints. Once equilibrated, both systems were subjected to 500-ns NPT MD in triplicate with a time step of 2 fs, resulting in a total of 1.5 μs for each of the systems. All bonds involving hydrogen atoms were treated using SHAKE (53) and long-range Coulomb interactions were handled with the smooth particle mesh Ewald method using a 10-Å cutoff for non-bonded interactions.

Trajectory analysis

The CPPTRAJ (54) module of AMBER18 was used to analyze the production trajectories. These analyses include the RMSD and correlation matrices. NMA was performed using ProDy (55). Various Python and R libraries were used to organize and analyze the raw data and Gnuplot (56) and Matplotlib (57) were used to put the data into a graphical format. EDA can be used to calculate the non-bonded interactions (Coulomb and van der Waals) to qualitatively assess the stabilizing or destabilizing role of different amino acids in a variety of protein systems (58–60) both for MD and QM/MM calculations. Amber-EDA was used to calculate these interactions with respect to specific residue sites using an in-house Fortran90 code (61). For this study, the analyses were run in three replicates of WT and the R853A mutant, and the results were averaged over the three systems. The residues chosen as reference were the incoming nucleotide and the mutation site Arg/Ala⁸⁵³. The protein system was separated into Palm, Fingers, and Thumb domains and the structural analyses were only done on the domains present in the crystal structure so that the extra flexibility from the modeled loops do not influence the data.

Experimental replicas

Activity assay and MD simulations were repeated three times. The results of each replicate of the MD simulations are shown in fig. S11.

Supplementary Materials

This PDF file includes:

Figs. S1 to S9

Table S1

Legend for movie S1

Other Supplementary Material for this manuscript includes the following:

Movie S1

REFERENCES AND NOTES

1. A. A. Johnson, Y. Tsai, S. W. Graves, K. A. Johnson, Human mitochondrial DNA polymerase holoenzyme: Reconstitution and characterization. *Biochemistry* **39**, 1702–1708 (2000).
2. M. J. Longley, P. A. Ropp, S. E. Lim, W. C. Copeland, Characterization of the native and recombinant catalytic subunit of human DNA polymerase gamma: Identification of residues critical for exonuclease activity and dideoxynucleotide sensitivity. *Biochemistry* **37**, 10529–10539 (1998).
3. K. G. Pinz, D. F. Bogenhagen, Characterization of a catalytically slow AP lyase activity in DNA polymerase γ and other family A DNA polymerases. *J. Biol. Chem.* **275**, 12509–12514 (2000).
4. K. L. DeBalsi, K. E. Hoff, W. C. Copeland, Role of the mitochondrial DNA replication machinery in mitochondrial DNA mutagenesis, aging and age-related diseases. *Ageing Res. Rev.* **33**, 89–104 (2017).
5. L.-J. C. Wong, R. K. Naviaux, N. Brunetti-Pierri, Q. Zhang, E. S. Schmitt, C. Truong, M. Milone, B. H. Cohen, B. Wical, J. Ganesh, A. A. Basinger, B. K. Burton, K. Swoboda, D. L. Gilbert, A. Vanderver, R. P. Saneto, B. Maranda, G. Arnold, J. E. Abdenur, P. J. Waters, W. C. Copeland, Molecular and clinical genetics of mitochondrial diseases due to POLG mutations. *Hum. Mutat.* **29**, E150–E172 (2008).
6. J. D. Stewart, S. Tennant, H. Powell, A. Pyle, E. L. Blakely, L. He, G. Hudson, M. Roberts, D. du Plessis, D. Gow, L. D. Mewasingh, M. G. Hanna, S. Omer, A. A. Morris, R. Roxburgh, J. H. Livingston, R. McFarland, D. M. Turnbull, P. F. Chinnery, R. W. Taylor, Novel POLG1 mutations associated with neuromuscular and liver phenotypes in adults and children. *J. Med. Genet.* **46**, 209–214 (2009).
7. A. R. Mehta, S. H. Fox, M. Tarnopolsky, G. Yoon, Mitochondrial mimicry of multiple system atrophy of the cerebellar subtype. *Mov. Disord.* **26**, 753–755 (2011).
8. O. Hikmat, K. Naess, M. Engvall, C. Klingenberg, M. Rasmussen, C. M. Tallaksen, E. Brodtkorb, E. Ostergaard, I. F. M. de Co, L. Pias-Peteiro, P. Isohanni, J. Uusimaa, N. Darin, S. Rahman, L. A. Bindoff, Simplifying the clinical classification of polymerase gamma (POLG) disease based on age of onset; studies using a cohort of 155 cases. *J. Inher. Metab. Dis.* **43**, 726–736 (2020).
9. S. Tang, J. Wang, N.-C. Lee, M. Milone, M. C. Halberg, E. S. Schmitt, W. J. Craig, W. Zhang, L.-J. C. Wong, Mitochondrial DNA polymerase γ mutations: An ever expanding molecular and clinical spectrum. *J. Med. Genet.* **48**, 669–681 (2011).
10. R. Kasiviswanathan, M. J. Longley, S. S. L. Chan, W. C. Copeland, Disease mutations in the human mitochondrial DNA polymerase thumb subdomain impart severe defects in mitochondrial DNA replication. *J. Biol. Chem.* **284**, 19501–19510 (2009).
11. J. Park, G. K. Herrmann, P. G. Mitchell, M. B. Sherman, Y. W. Yin, Poly coordinates DNA synthesis and proofreading to ensure mitochondrial genome integrity. *Nat. Struct. Mol. Biol.* **30**, 812–823 (2023).
12. M. R. Szymanski, V. B. Kuznetsov, C. Shumate, Q. Meng, Y. S. Lee, G. Patel, S. Patel, Y. W. Yin, Structural basis for processivity and antiviral drug toxicity in human mitochondrial DNA replicase. *EMBO J.* **34**, 1959–1970 (2015).
13. Y. S. Lee, W. D. Kennedy, Y. W. Yin, Structural insight into processive human mitochondrial DNA synthesis and disease-related polymerase mutations. *Cell* **139**, 312–324 (2009).
14. M. van Heel, M. Schatz, Fourier shell correlation threshold criteria. *J. Struct. Biol.* **151**, 250–262 (2005).
15. T. A. Steitz, Y. W. Yin, Accuracy, lesion bypass, strand displacement and translocation by DNA polymerases. *Philos. Trans. R. Soc. Lond. B Biol. Sci.* **359**, 17–23 (2004).
16. M. F. Goodman, S. Creighton, L. B. Bloom, J. Petruska, Biochemical basis of DNA replication fidelity. *Crit. Rev. Biochem. Mol. Biol.* **28**, 83–126 (1993).
17. J. L. Ong, D. Loakes, S. Jaroslowski, K. Too, P. Holliger, Directed evolution of DNA polymerase, RNA polymerase and reverse transcriptase activity in a single polypeptide. *J. Mol. Biol.* **361**, 537–550 (2006).
18. A. M. DeLucia, S. Chaudhuri, O. Potapova, N. D. Grindley, C. M. Joyce, The properties of steric gate mutants reveal different constraints within the active sites of Y-family and A-family DNA polymerases. *J. Biol. Chem.* **281**, 27286–27291 (2006).
19. J. Balzarini, K. Das, J. A. Bernatchez, S. E. Martinez, M. Ngure, S. Keane, A. Ford, N. Maguire, N. Mullins, J. John, Y. Kim, W. Dehaen, J. Vande Voorde, S. Liekens, L. Naesens, M. Gotte, A. R. Maguire, E. Arnold, Alpha-carboxy nucleoside phosphonates as universal nucleoside triphosphate mimics. *Proc. Natl. Acad. Sci. U.S.A.* **112**, 3475–3480 (2015).
20. S. D. McCulloch, T. A. Kunkel, The fidelity of DNA synthesis by eukaryotic replicative and translesion synthesis polymerases. *Cell Res.* **18**, 148–161 (2008).
21. T. A. Kunkel, K. Bebenek, DNA replication fidelity. *Annu. Rev. Biochem.* **69**, 497–529 (2000).
22. G. Yang, M. Franklin, J. Li, T. C. Lin, W. Konigsberg, Correlation of the kinetics of finger domain mutants in RB69 DNA polymerase with its structure. *Biochemistry* **41**, 2526–2534 (2002).
23. J. Petruska, M. F. Goodman, M. S. Boosalis, L. C. Sowers, C. Cheong, I. Tinoco Jr., Comparison between DNA melting thermodynamics and DNA polymerase fidelity. *Proc. Natl. Acad. Sci. U.S.A.* **85**, 6252–6256 (1988).
24. A. H. Polesky, M. E. Dahlberg, S. J. Benkovic, N. D. Grindley, C. M. Joyce, Side chains involved in catalysis of the polymerase reaction of DNA polymerase I from *Escherichia coli*. *J. Biol. Chem.* **267**, 8417–8428 (1992).
25. A. H. Polesky, T. A. Steitz, N. D. Grindley, C. M. Joyce, Identification of residues critical for the polymerase activity of the Klenow fragment of DNA polymerase I from *Escherichia coli*. *J. Biol. Chem.* **265**, 14579–14591 (1990).
26. D. T. Minnick, K. Bebenek, W. P. Osheroff, R. M. Turner Jr., M. Astatke, L. Liu, T. A. Kunkel, C. M. Joyce, Side chains that influence fidelity at the polymerase active site of *Escherichia coli* DNA polymerase I (Klenow fragment). *J. Biol. Chem.* **274**, 3067–3075 (1999).
27. A. S. Meyer, M. Blandino, T. E. Spratt, *Escherichia coli* DNA polymerase I (Klenow fragment) uses a hydrogen-bonding fork from Arg668 to the primer terminus and incoming deoxynucleotide triphosphate to catalyze DNA replication. *J. Biol. Chem.* **279**, 33043–33046 (2004).
28. C. A. Brautigam, H. Zhao, C. Vargas, S. Keller, P. Schuck, Integration and global analysis of isothermal titration calorimetry data for studying macromolecular interactions. *Nat. Protoc.* **11**, 882–894 (2016).
29. Z. Otwinowski, W. Minor, *Methods in Enzymology*, C. W. J. Carter, R. M. Sweet, Eds. (Academic Press, 1997), vol. 276, pp. 307–326.
30. A. Casañal, B. Lohkamp, P. Emsley, Current developments in Coot for macromolecular model building of electron cryo-microscopy and crystallographic data. *Protein Sci.* **29**, 1069–1078 (2020).
31. D. Liebschner, P. V. Afonine, M. L. Baker, G. Bunkóczi, V. B. Chen, T. I. Croll, B. Hintze, L. W. Hung, S. Jain, A. J. McCoy, N. W. Moriarty, R. D. Oeffner, B. K. Poon, M. G. Prisant, R. J. Read, J. S. Richardson, D. C. Richardson, M. D. Sammito, O. V. Sobolev, D. H. Stockwell, T. C. Terwilliger, A. G. Urzhumtsev, L. L. Videau, C. J. Williams, P. D. Adams, Macromolecular structure determination using X-rays, neutrons and electrons: Recent developments in Phenix. *Acta Crystallogr. D Struct. Biol.* **75**, 861–877 (2019).
32. A. Punjani, J. L. Rubinstein, D. J. Fleet, M. A. Brubaker, cryoSPARC: Algorithms for rapid unsupervised cryo-EM structure determination. *Nat. Methods* **14**, 290–296 (2017).
33. J. Zivanov, T. Nakane, S. H. W. Scheres, Estimation of high-order aberrations and anisotropic magnification from cryo-EM data sets in RELION-3.1. *IUCr J.* **7**, 253–267 (2020).
34. A. Punjani, H. Zhang, D. J. Fleet, Non-uniform refinement: Adaptive regularization improves single-particle cryo-EM reconstruction. *Nat. Methods* **17**, 1214–1221 (2020).

35. G. Cardone, J. B. Heymann, A. C. Steven, One number does not fit all: Mapping local variations in resolution in cryo-EM reconstructions. *J. Struct. Biol.* **184**, 226–236 (2013).
36. E. F. Pettersen, T. D. Goddard, C. C. Huang, E. C. Meng, G. S. Couch, T. I. Croll, J. H. Morris, T. E. Ferrin, UCSF ChimeraX: Structure visualization for researchers, educators, and developers. *Protein Sci.* **30**, 70–82 (2021).
37. S. Kaur, J. Gomez-Blanco, A. A. Z. Khalifa, S. Adinarayanan, R. Sanchez-Garcia, D. Wrapp, J. S. McLellan, K. H. Bui, J. Vargas, Local computational methods to improve the interpretability and analysis of cryo-EM maps. *Nat. Commun.* **12**, 1240 (2021).
38. E. F. Pettersen, T. D. Goddard, C. C. Huang, G. S. Couch, D. M. Greenblatt, E. C. Meng, T. E. Ferrin, UCSF Chimera—A visualization system for exploratory research and analysis. *J. Comput. Chem.* **25**, 1605–1612 (2004).
39. P. Emsley, K. Cowtan, Coot: Model-building tools for molecular graphics. *Acta Crystallogr. D Biol. Crystallogr.* **60**, 2126–2132 (2004).
40. T. I. Croll, ISOLDE: A physically realistic environment for model building into low-resolution electron-density maps. *Acta Crystallogr. D Struct. Biol.* **74**, 519–530 (2018).
41. C. J. Williams, J. J. Headd, N. W. Moriarty, M. G. Prisant, L. L. Videau, L. N. Deis, V. Verma, D. A. Keedy, B. J. Hintze, V. B. Chen, S. Jain, S. M. Lewis, W. B. Arendall III, J. Snoeyink, P. D. Adams, S. C. Lovell, J. S. Richardson, D. C. Richardson, MolProbity: More and better reference data for improved all-atom structure validation. *Protein Sci.* **27**, 293–315 (2018).
42. G. Pintilie, K. Zhang, Z. Su, S. Li, M. F. Schmid, W. Chiu, Measurement of atom resolvability in cryo-EM maps with Q-scores. *Nat. Methods* **17**, 328–334 (2020).
43. C. A. Rohl, C. E. M. Strauss, K. M. S. Misura, D. Baker, Protein structure prediction using Rosetta. *Methods Enzymol.* **383**, 66–93 (2004).
44. W. Humphrey, A. Dalke, K. Schulten, VMD: Visual molecular dynamics. *J. Mol. Graph.* **14**, 33–38 (1996).
45. N. M. Antczak, A. R. Walker, H. R. Stern, E. M. Leddin, C. Palad, T. A. Coulther, R. J. Swett, G. A. Cisneros, P. J. Beuning, Characterization of nine cancer-associated variants in human DNA polymerase κ . *Chem. Res. Toxicol.* **31**, 697–711 (2018).
46. M. H. M. Olsson, C. R. Søndergaard, M. Rostkowski, J. H. Jensen, PROPKA3: Consistent treatment of internal and surface residues in empirical pKa predictions. *J. Chem. Theory Comput.* **7**, 525–537 (2011).
47. C. Schafmeister, W. Ross, V. Romanovski, LeAP. University of California, San Francisco (1995).
48. J. A. Maier, C. Martinez, K. Kasavajhala, L. Wickstrom, K. E. Hauser, C. Simmerling, ff14SB: Improving the accuracy of protein side chain and backbone parameters from ff99SB. *J. Chem. Theory Comput.* **11**, 3696–3713 (2015).
49. J. Wang, R. M. Wolf, J. W. Caldwell, P. A. Kollman, D. A. Case, Development and testing of a general amber force field. *J. Comput. Chem.* **25**, 1157–1174 (2004).
50. R. Galindo-Murillo, J. C. Robertson, M. Zgarbová, J. Šponer, M. Otyepka, P. Jurečka, T. E. Cheatham III, Assessing the current state of amber force field modifications for DNA. *J. Chem. Theory Comput.* **12**, 4114–4127 (2016).
51. D. A. Case, I. Y. Ben-Shalom, S. R. Brozell, D. S. Cerutti, T. E. Cheatham, III, V. W. D. Cruzeiro, T. A. Darden, R. E. Duke, D. Ghoreishi, M. K. Gilson, H. Gohlke, A. W. Goetz, D. Greene, R. Harris, N. Homeyer, Y. Huang, S. Izadi, A. Kovalenko, T. Kurtzman, T. S. Lee, S. LeGrand, P. Li, C. Lin, J. Liu, T. Luchko, R. Luo, D. J. Mermelstein, K. M. Merz, Y. Miao, G. Monard, C. Nguyen, H. Nguyen, I. Omelyan, A. Onufriev, F. Pan, R. Qi, D. R. Roe, A. Roitberg, C. Sagui, S. Schott-Verdugo, J. Shen, C. L. Simmerling, J. Smith, R. Salomon-Ferrer, J. Swails, R. C. Walker, J. Wang, H. Wei, R. M. Wolf, X. Wu, L. Xiao, D. M. York, P. A. Kollman, AMBER18. University of California, San Francisco (2018).
52. R. J. Loncharich, B. R. Brooks, R. W. Pastor, Langevin dynamics of peptides: The frictional dependence of isomerization rates of N-acetylalanyl-N'-methylamide. *Biopolymers* **32**, 523–535 (1992).
53. J. Ryckaert, J. Ciccotti, H. J. C. Berendsen, Numerical integration of the cartesian equations of motion of a system with constraints: Molecular dynamics of n-alkanes. *J. Comput. Phys.* **23**, 327–341 (1976).
54. D. R. Roe, T. E. Cheatham, PTRAJ and CPPTRAJ: Software for processing and analysis of molecular dynamics trajectory data. *J. Chem. Theory Comput.* **9**, 3084–3095 (2013).
55. S. Zhang, J. M. Krieger, Y. Zhang, C. Kaya, B. Kaynak, K. Mikulska-Ruminska, P. Doruker, H. Li, I. Bahar, ProDy 2.0: Increased scale and scope after 10 years of protein dynamics modelling with python. *Bioinformatics* **37**, 3657–3659 (2021).
56. T. Williams, C. Kelley, H. Broker, R. John Campbell, D. Cunningham, G. Denholm, R. Elber, C. Fearick, L. Grammes, L. Hart, An interactive plotting program, *Gnuplot* (2017); www.gnuplot.info/docs_4.0/gnuplot.html.
57. J. D. Hunter, Matplotlib: A 2D graphics environment. *Comput. Sci. Eng.* **9**, 90–95 (2007).
58. M. B. Berger, G. A. Cisneros, Distal mutations in the β -clamp of DNA polymerase III* disrupt DNA orientation and affect exonuclease activity. *J. Am. Chem. Soc.* **145**, 3478–3490 (2023).
59. H. M. Senn, D. O'Hagan, W. Thiel, Insight into enzymatic C-F bond formation from QM and QM/MM calculations. *J. Am. Chem. Soc.* **127**, 13643–13655 (2005).
60. Y. Maghsoud, C. Dong, G. A. Cisneros, Computational characterization of the inhibition mechanism of xanthine oxidoreductase by topiroxostat. *ACS Catal.* **13**, 6023–6043 (2023).
61. E. Leddin; Cisneros Research Group, G. A. Cisneros, CisnerosResearch/Amber-Eda: Updated stddev calculation. *Zenodo* (2021); <https://zenodo.org/records/4469899>, DOI:10.5281/zenodo.4469899.

Acknowledgments: We would like to thank W. Chiu and P. Mitchell for invaluable support and T. Lucas for helpful preliminary studies. **Funding:** The work is supported by NIH grants (R01AI134611 and R01GM145925 to Y.W.Y. and R01GM108583 to G.A.C.), the Jeane B. Kempner postdoctoral fellowship to J.P., and an endowment from the Sealy and Smith Foundation to the Sealy Center for Structural Biology and Molecular Biophysics at UTMB. Computational time was provided by UT Dallas CIT HPC facilities and the University of North Texas CASCaM CRUNTC3 high-performance cluster supported by NSF grant nos. CHE-1531468 and OAC-2117247. The work at Lawrence Berkeley National Laboratory is supported by the Office of Science, Office of Basic Energy Sciences of the U.S. Department of Energy (contract no. DE-AC02-05CH11231). Stanford-SLAC Cryo-EM Center (S^2C^2) is supported by the NIH Common Fund Transformative High-Resolution Cryo-Electron Microscopy program (U24 GM129541). **Author contributions:** Conceptualization: Y.W.Y. and G.A.C. Investigation: J.P., G.K.H., A.R., and C.K.S. Supervision: Y.W.Y. and G.A.C. Writing—original draft: J.P., G.K.H., and A.R. Writing—review and editing: J.P., G.K.H., A.R., Y.W.Y., and G.A.C. **Competing interests:** The authors declare that they have no competing interests. **Data and materials availability:** Cryo-EM density map and corresponding coordinate of wild-type Pol γ binary complex have been deposited in the Worldwide Protein Data Bank (wwPDB) OneDep System under the following accession codes: EMD-42150 and PDB: 8UDL. The coordinate of the Pol γ R853A ternary complex has been deposited in the Protein Data Bank with accession code PDB: 8UDK. The computational data supporting the findings in this study have been deposited to the Zenodo repository (doi:10.5281/zenodo.8377289). Combined and water-stripped netcdf files consisting of 100 ns (10,000 frames) of the representative replicates have been deposited for both the WT and the R853A mutant systems, along with the last 1-ns (100 frames) unstripped trajectories. The stripped and solvated parameter files of both systems have also been deposited. All other data needed to evaluate the conclusions in the paper are present in the paper and/or the Supplementary Materials.

Submitted 12 October 2023

Accepted 18 April 2024

Published 24 May 2024

10.1126/sciadv.adl3214